From breast cancer cell homing to the onset of early bone metastasis: dynamic bone (re)modeling as a driver of metastasis

Sarah A. E. Young[1], Anna-Dorothea Heller[1], Daniela S. Garske[1], Maximilian Rummler[1,2], Victoria Qian[1], Agnes Ellinghaus[3], Georg N. Duda[3], Bettina M. Willie[2], Anika Grüneboom[4], Amaia Cipitria[1,5,6 (*)]

[1] Department of Biomaterials, Max Planck Institute of Colloids and Interfaces, Potsdam, Germany

[2] Research Centre, Shriners Hospital for Children - Canada, Faculty of Dental Medicine and Oral Health Sciences, McGill University, Montreal, Canada

[3] Julius Wolff Institute, Berlin Institute of Health at Charité – Universitätsmedizin Berlin, Germany

[4] Leibniz-Institute for Advancing Analytics – ISAS – e.V., Dortmund, Germany

[5] Group of Bioengineering in Regeneration and Cancer, Biodonostia Health Research Institute, San Sebastian, Spain

[6] IKERBASQUE, Basque Foundation for Science, Bilbao, Spain

(*) Corresponding author: amaia.cipitria@mpikg.mpg.de

Phone number: +49 331 567-9452

Max Planck Institute of Colloids and Interfaces, Am Mühlenberg 1, 14476 Potsdam

Abstract:

Breast cancer often metastasizes to bone causing osteolytic lesions. Structural and biophysical changes are rarely studied, yet are hypothesized to influence metastatic progression. Here, we developed a mouse model of early bone metastasis and multimodal 3D imaging to quantify cancer cell homing, dynamic bone (re)modeling and onset of bone metastasis. Using 3D light sheet fluorescence microscopy, we show eGFP^{+} cancer cells and small clusters in 3D (intact) bones. We detect early bone lesions using time-lapse *in vivo* microCT and reveal altered bone (re)modeling in absence of detectable lesions. With a new microCT image analysis tool, we detect and track the growth of early bone lesions over time. We show that cancer cells home in all bone compartments, while osteolytic lesions are only detected in the metaphysis, a region of high (re)modeling. Our study provides novel insights of dynamic bone (re)modeling as a driver during the early phase of metastasis.

Keywords:

Breast cancer bone metastasis; Dynamic bone (re)modeling; Early bone osteolytic lesion; 3D light-sheet fluorescence microscopy (LSFM); *In vivo* microCT time-lapse morphometry; Multiscale correlative tissue characterization

Introduction

Bone metastases often originate from breast cancer, one of the leading causes for cancer-associated deaths among women worldwide[1]. 65-80% of patients with advanced breast cancer develop bone metastasis[2,3]. Breast cancer cells homing to bone lead to osteolytic lesions[2] and drastically lower the prognosis of survival[4]. Metastatic cancer undergoes different stages of activity, from a dormant invisible stage that can last up to decades, to small growing metastases and up to advanced overt metastasis and skeletal morbidity[5–7]. Much work has been reported on primary tumor growth and advanced overt metastasis, but less is known about the early phases of metastasis, such as the premetastatic niche[8], the antimetastatic niche[9], the dormant niche[10] or the early metastatic niche[11].

The biophysical and structural properties of the tumor microenvironment have become a key focus of research. Advanced physical science methods hold great potential to reveal physico-chemical alterations that modulate early phases of metastasis. A recent study showed that the extracellular matrix (ECM) composed of tumor-derived collagen type III sustained tumor cell dormancy, and changes in its architecture and density restored proliferation [12]. As another ECM protein, fibronectin fibers were found to be under lower tension in tumor invaded tissues compared to healthy tissue[13]. In the context of mineralized bone tissue, mineral nanocrystals composed of less-mature hydroxyapatite were associated with the initiation of metastasis [11]. A follow-up study recapitulated the premetastatic niche by systemic injection of tumor conditioned media, which induced increased bone formation of altered quality[8] and suggested potential consequences on the initial seeding of breast cancer cells. However, multimodal 3D imaging is required to shed light on the tight interlink between tissue structural changes and cancer progression during early phases of metastasis. This is particularly challenging in mineralized

64 bone tissue, since it is less accessible than soft organs and imaging of soft bone marrow
65 compartments within 3D intact bones requires advanced multimodal 3D imaging methods[14,15].
66 The dynamics of matrix (re)modeling is another key aspect of metastatic progression[16]. Bone is a
67 highly dynamic organ and mineralized tissue is constantly (re)modelled[17]. The differences in
68 bone turnover between young and older animals did not affect the seeding of breast cancer cells
69 but influenced the development of overt osteolytic bone metastasis: young mice with higher bone
70 turnover exhibited higher numbers of overt skeletal lesions, as quantified by histology and *ex*
71 *vivo* microcomputed tomography (microCT)[18]. Another study used longitudinal *in vivo* microCT
72 to investigate the altered bone tissue dynamics due to metastasis and quantified bulk bone
73 destruction upon direct intratibial injection of cancer cells[19]. However, the spatial resolution of
74 the *in vivo* microCT scans limited the quantitative analysis to large bone lesions during advanced
75 overt metastasis. In this context, we have recently described quantitatively anatomical site-
76 specific differences in bone (re)modeling of healthy 12-week-old skeletally mature mice, with
77 the metaphysis (in femur and tibia) being the region of highest bone (re)modeling and the tibia
78 being more (re)modeled than the femur[20]. Furthermore, this served as baseline to detect the onset
79 of bone pathologies, taking breast cancer metastasis as proof-of-concept[20]. Understanding the
80 dynamics of bone (re)modeling and correlating this with the visualization and quantification of
81 homing of breast cancer cells, will shed light on the role of bone tissue dynamics on breast
82 cancer cell homing and/or on initiation of osteolytic lesions.
83 We hypothesized that the dynamic microenvironment in the bone drives the progression of early
84 bone metastasis. Therefore, we established an experimental breast cancer bone metastasis mouse
85 model to study the early stages of metastasis, from breast cancer cell homing to the onset of early
86 bone lesions, both *in vivo* and *ex vivo*. Skeletally mature 12-week-old female BALB/c nude mice

87 were injected intracardially with eGFP$^+$ bone-tropic breast cancer cells, to recapitulate the stage
88 of disseminated cancer cells in circulation. We visualized and quantified the homing of breast
89 cancer cells and small clusters to the bone marrow with advanced light-sheet fluorescence
90 microscopy (LSFM) using 3D (intact) long bones. LSFM revealed breast cancer cells and small
91 clusters disseminated to all bones and different compartments. Dynamic bone (re)modeling was
92 investigated by *in vivo* microCT-based time-lapse morphometry and revealed altered bone
93 (re)modeling in absence of detectable bone lesions. The method was further adapted and we
94 developed a new image analysis tool to detect and track the growth of early bone lesions over
95 time. Osteolytic lesions occurred in characteristics locations of high bone (re)modeling activity
96 in the metaphysis, in both cortical and trabecular bone; no lesion was detected in the epiphysis or
97 diaphysis. In addition, we used advanced *ex vivo* multimodal methods to characterize the
98 structural changes caused by early lesions. Altogether, the results suggest that dynamic bone
99 (re)modeling is a driver of metastasis, as breast cancer cells reach every bone compartment, yet
100 lesions only occur in the dynamic regions like the metaphysis. Our study provides novel insights
101 of dynamic bone (re)modeling in metastatic initiation and progression.
102
103 **Results**
104 **Breast cancer cells and small clusters homing in the bone marrow visualized by 3D light-**
105 **sheet fluorescence microscopy**
106 LSFM was used to study the homing of breast cancer cells and small cell clusters in 3D (intact)
107 tibiae. Optical clearing makes the bone transparent to LSFM and allows 3D visualization of
108 fluorescently labeled (eGFP$^+$) breast cancer cells in the bone marrow and in the periosteum. The
109 (virtual) 2D section overview image in Fig. 1A shows breast cancer cells and small cell clusters

110 infiltrating the entire bone marrow of the tibia (Fig. 1A.1-2) (Supplementary Movie 1). In
111 addition, larger and denser clusters of cancer cells were found in the periosteal region
112 (Fig. 1A.3). Single cells and small clusters of only a few cells were found in between muscle
113 tissue and all over the periosteal bone surface (Fig. 1A.4). The quantitative analysis of the size
114 and spatial distribution of around 5,500 cells and cell clusters in the bone marrow of five
115 different bones (Fig. 1F) shows that most breast cancer cells are in close proximity to the cortical
116 bone surface (Supplementary Movie 2), with a mean distance of around 50 µm (Fig. 1C) and a
117 mean diameter ranging between 31-36 µm (Fig. 1D). Periosteal cell clusters on the other hand
118 can be much larger with volumes up to 0.1 mm^3 (Fig. 1E).
119 Further descriptive analysis of the homing of breast cancer cells and small clusters revealed that
120 these are detected in all bone compartments like the diaphysis, metaphysis and epiphysis, as well
121 as in different types of bone such as tibia and fibula, as shown in Fig. 2.
122
123 **Detection and tracking of the growth of early bone metastatic lesions over time**
124 To detect the location and track the growth of early metastatic lesions over time in cortical bone,
125 a new image analysis tool was developed, using *in vivo* microCT-based time-lapse morphometry.
126 Dynamic bone (re)modeling was investigated by overlapping a reference scan (4 days prior to
127 cancer cell injection) with later time points. The resulting visualization of constant bone
128 (yellow), newly mineralized bone (blue) and eroded bone (red) can be quantified in volume,
129 surface and apposition/resorption rate[20,21].
130 Our new image analysis tool has the ability to differentiate between physiological and
131 pathological erosion patches. The method is based on empirically determined threshold
132 parameters to define a 3D neighborhood by summing up eroded voxels as shown in Fig. 3A.

133 Briefly, a first noise filtering is performed and only eroded bone patches are considered, which
134 fulfill the criterion that 70% of the neighborhood (respectively 3 voxels in positive and negative
135 x-, y- and z-direction) consists of erosion voxels (Fig. 3B). Next, to distinguish physiological vs.
136 pathological erosion patches, we search for the pathological eroded bone patch core, which
137 fulfills the stricter criterion that 92% of a larger neighborhood (respectively 9 voxels in positive
138 and negative x-, y-direction, 4 voxels in positive and negative z-direction) consists of eroded
139 voxels (Fig. 3C). Finally, the volume of the pathological eroded bone patch is determined by the
140 noise-filtered eroded bone patch including the patch core (Fig. 3D). The threshold settings were
141 obtained and validated with datasets from PBS-injected control animals with physiological bone
142 (re)modeling, confirming that no pathological eroded bone patches were detected.
143 Osteolytic erosion patches were found in the cortical bone of six animals, with three in the tibia
144 and three in the femur as shown in Fig. 4 and one exemplary osteolytic lesion in Supplementary
145 Movie 3 and Movie 4. Five of these lesions started on the periosteal bone surface, suggesting an
146 onset in that region (Fig. 4A, B, D) and one in the endocortical bone (Fig. 4C). All lesions were
147 detected as early as day 17, which is the first time point that was measured after the reference
148 scan (day 0, four days prior to cancer cell injection). The patch size at first detection varied
149 between 0.005 – 0.025 mm^3, with equal distribution of smaller and bigger lesions in both femur
150 and tibia. Lesions were tracked for up to 27 days (animal sacrifice due to humane endpoint
151 criteria). In several animals the osteolytic eroded bone patch volume increased, with the clearest
152 example being animal 1 starting at 0.01 mm^3 and reaching a final lesion volume of nearly
153 0.1 mm^3 (Fig. 4E). The eroded bone patch analysis enables the spatio-temporal visualization and
154 quantification of early osteolytic lesions, which provides fundamental understanding of the onset
155 of bone metastasis.

156 **Metastatic lesions in trabecular bone initiate on the mineralized surface adjacent to the**
157 **growth plate**

158 Metastatic osteolytic lesions in trabecular bone were visually detected in the primary spongiosa,
159 right on the mineralized surface adjacent to the growth plate, mainly in the tibia (Fig. 5A-C) but
160 also in the femur (Fig. 5D). For all lesions, a top view and enlargements of a cross section are
161 shown, both as bone (re)modeling analysis data and the respective grey scale image. The
162 enlarged images (Fig. 5A.1-D.1) confirm that the growth plate is eroded in a larger area,
163 spanning both along the growth plate and towards the secondary spongiosa. Although all lesions
164 are still at a very early stage, Fig. 5B.1 clearly shows the smallest lesion with a diameter along
165 the growth plate of under 200 µm. Two of the lesions are right between the condyles (Fig. 5A
166 and D), the others do not show any distinct pattern.

167 To summarize, we were able to identify the onset of metastatic bone lesions visualized with
168 microCT-based time-lapse morphometry, on both cortical and trabecular bone. Based on the
169 location where they initiate, we identify: (i) fully cortical lesions that start on the periosteal side
170 and do not reach the trabecular bone even after growing for 10 days (Fig. 4A); (ii) mixed lesions
171 where both the endocortical bone (Fig. 4C) and adjacent trabecular bone are resorbed (Fig. 5D);
172 (iii) fully trabecular lesions located directly at the mineralized growth plate in the metaphysis
173 (Fig. 5).

174

175 **Structural microenvironment of early metastatic bone lesions visualized with multiscale**
176 **correlative tissue characterization**

177 The early metastatic bone lesions detected with microCT-based time-lapse morphometry were
178 then subjected to multiscale correlative tissue characterization to evaluate the structural

179 microenvironment. Cortical and trabecular bone osteolytic lesions in femur (Fig. 6A-I) and tibia
180 (Fig. 6J-R) were analyzed and compared with intact regions within the same bone.
181 An overview image of the femur using backscattered electron (BSE) microscopy is shown in
182 Fig. 6A, with the mineralized tissue of the bone being intact except for the cortical lesion in the
183 posterior metaphysis (enlargement in Fig. 6B). The cortical bone is resorbed across nearly the
184 entire cortical thickness, with only a thin layer remaining on the endocortical side. In the
185 progression of such early osteolytic lesions, the matrix containing the lacuno-canalicular network
186 is resorbed (Fig. 6C). The collagen analysis with second-harmonic generation (SHG) imaging
187 also shows that all fibrillar collagen type I fibers that were part of the cortical bone have been
188 resorbed (Fig. 6D). Interestingly, the thick collagen layer in the periosteum is still intact
189 (Fig. 6D). The lesion region is now filled with a new soft tissue with high density of cells
190 (Fig. 6C, E).
191 Similarly, an overview image of the tibia using BSE microscopy is shown in Fig. 6J, with the
192 mineralized tissue of the bone being intact except for the trabecular lesion on the anterior growth
193 plate (enlargement in Fig. 6K). The mineralized part of the growth plate is visibly thinned out in
194 that region and the surrounding trabeculae show a rough surface, indicating an ongoing erosion
195 of the tissue. In analogy to the cortical lesion, the matrix containing the lacuno-canalicular
196 network (Fig. 6L) and fibrillar collagen type I fibers (Fig. 6M) are fully resorbed, while the
197 growth plate on the posterior side (Fig. 6O-R) is fully intact.
198 In summary, in both early cortical and trabecular lesions, the mineralized tissue, including
199 embedded lacunae and canaliculi, as well as collagen fibers within mineralized tissue are all fully
200 resorbed and replaced by a new soft tissue with high density of cells.
201

202 **Breast cancer cells and small clusters homing in the bone marrow have a tendency for low**
203 **proliferation**
204 The proliferation state of the breast cancer cells and small clusters in the bone marrow was
205 analyzed using the proliferation marker Ki67. Sections from three bones harvested from three
206 tumor animals, exhibiting an osteolytic lesion in at least one bone, were imaged. In total 364
207 breast cancer cells or small clusters were detected inside the bone marrow (Fig. 7A with
208 enlargements in A.1, and A.2) and analyzed for the proliferation status (Fig. 7B). A cluster of
209 cells was counted as $Ki67^+$ as soon as one cell in this cluster was positive. High resolution
210 examples of $Ki67^+$ (Fig. 7A.1) and $Ki67^-$ (Fig. 7A.2) are shown and single channel views are
211 included in Fig. S1. We show that half of the single cells and small clusters are $Ki67^-$, while
212 those considered as $Ki67^+$ typically entail only one $Ki67^+$ cell. We conclude that at early stages
213 of breast cancer homing to the bone marrow, single cells and small clusters have a tendency for
214 low proliferation.
215
216 **Breast cancer cells and small clusters are found in close proximity to and inside of blood**
217 **vessels**
218 The distance of individual breast cancer cells and small clusters to blood vessels in the bone
219 marrow stained with the CD31 endothelial cell marker was analyzed with the software Imaris
220 (Fig. 7E). Sections from four bones harvested from four tumor animals, with an osteolytic lesion
221 in at least one hind limb were analyzed. Most cancer cells can be found in direct contact with
222 blood vessels and only few at further distance, with a maximum distance at 16 µm (Fig. 7C).
223 Breast cancer cells are overlapping with blood vessel to a different extent as quantified in
224 Fig. 7D, from 100% overlap (Fig. 7E.1), to partial overlap (Fig. 7E.2) or no overlap (Fig. 7E.3).

225 In addition, cancer cells are found close to the endocortical bone surface, which is also a highly
226 vascularized region (Fig. 7E.4).
227
228 **Homing of breast cancer cells in the bone marrow enhances new mineralization in the**
229 **absence of detectable osteolytic lesions**
230 To study the effect of breast cancer cell homing in the dynamics of bone (re)modeling, we
231 investigated tumor animals without detectable osteolytic lesions (n = 5) up to 38 days and
232 compared with PBS-injected control animals (n = 7). The trabecular bone (re)modeling in the
233 tibia proximal metaphysis is shown in Fig. 8A-H. An exemplary image of a tumor animal is
234 depicted in Fig. 8A and the PBS-injected control animal in Fig. 8B. The corresponding
235 mineralized volume (MV/BV), surface (MS/BS), with the soft tissue interface (MS_{ST}/BS) and
236 constant bone interfaces (MS_{CB}/BS)[20] and mineral apposition rate (MAR) are shown in Fig. 8C-
237 E, while the eroded volume (EV/BV), surface (ES/BS), with the soft tissue interface (ES_{ST}/BS)
238 and constant bone interfaces (ES_{CB}/BS)[20] and mineral resorption rate (MRR) in Fig. 8F-H. The
239 tumor animal shows more newly mineralized trabecular bone and less eroded bone (Fig. 8A),
240 compared to the PBS-injected control animal.
241 Higher MV/BV is observed in the tumor animals at all time points (except day 17), with values
242 reaching between up to 1.5 – 2.5 for tumor animals, while it stays below 1 for PBS-injected
243 control animals, and showing significant differences after day 31 (Fig. 8C). Similar results are
244 observed for MS/BS (Fig. 8D), while the MAR is only significantly elevated at day 38 (Fig 8E).
245 Lower erosion in the tumor animals can be observed with EV/BV (Fig 8F) and ES/BS (Fig. 8G),
246 showing significant differences after day 34, and MRR (Fig. 8H) at day 17, 20, 31, 34 and 38.

247 Analogous analysis is performed in the femur distal metaphysis (Fig. 8I-P). Trabecular bone
248 volume, surface and apposition/resorption rate are shown in Fig. 8K-P, with exemplary images
249 for the tumor animals in Fig. 8I and PBS-injected control animals in Fig. 8J. Similar trends as in
250 the tibia are found in the femur, although the femur shows overall less (re)modeling. Similar
251 trends are also found in the cortical bone (Fig. S2), with overall less (re)modeling.
252
253 **Discussion**
254 In this study, we aimed to understand the role of biophysical and structural properties of the bone
255 microenvironment and its dynamics on the early phases of breast cancer bone metastasis. To do
256 so, we developed an early bone metastasis mouse model using skeletally mature 12-week-old
257 female BALB/c nude mice. We visualized and quantified the spatial distribution of disseminated
258 breast cancer cells in (intact) bone by 3D light sheet fluorescence microscopy. Further, we
259 quantified dynamic bone structural changes using *in vivo* microCT-based time-lapse
260 morphometry and developed an image analysis tool to detect and track early osteolytic lesions.
261 Combining multimodal advanced 3D imaging, we revealed that breast cancer cells disseminate
262 in all bone compartments, yet bone osteolytic lesions initiate in regions of high dynamic bone
263 (re)modeling. Our study provides novel insights of the interplay between dynamic bone
264 structural changes and metastasis initiation and progression.
265 Using tissue clearing and 3D light sheet fluorescence microscopy, we visualize for the first-time
266 $eGFP^+$ bone-tropic breast cancer cells and small clusters in (intact) 3D mineralized bones (Fig. 1)
267 and show that they home to all bone compartments, including the epiphysis, metaphysis and
268 diaphysis (Fig. 2). Quantitative analysis of their size and spatial distribution within the bone
269 marrow revealed that the breast cancer cells and small clusters range between 10-60 μm and are
270 in close proximity to bone surfaces. Larger clusters are found on the periosteum with a volume

271 of up to 0.1 mm^3. This might indicate that only small clusters or single cells can traverse
272 capillaries and home in the bone marrow. In addition, the large clusters on the periosteum could
273 be a sign of a more advanced stage of metastasis and are well in line with the osteolytic lesions
274 starting at the periosteum (Fig. 5). The ability of cancer cells to form clusters has been described
275 in the past and it was associated with a higher potential to survive and form lesions than single
276 cells[22].
277 In contrast with the finding that breast cancer cells home to all bone compartments, the
278 localization of osteolytic lesions is highly specific in regions of high bone (re)modeling like the
279 metaphyseal bone (Fig. 4-6), while no lesions were detected in the epiphysis or the diaphysis.
280 Therefore, the ability for breast cancer cells to home to the bone is not sufficient as an
281 explanation for the formation of osteolytic lesions. Cortical and trabecular bone in the
282 metaphysis undergoes more (re)modeling than the diaphysis[21] or the epiphysis[20]. This calls for a
283 new time dependent and dynamic criterion for metastatic initiation and progression. This is in
284 agreement with previous studies highlighting the importance of animal age in bone metastasis
285 progression: young mice with higher bone turnover exhibited higher numbers of overt skeletal
286 lesions, despite having comparable number of breast cancer cells disseminated to the bone as in
287 older animals[18]. In our study, we used skeletally mature 12-week-old mice. Yet, even in
288 skeletally mature mice, there are region-specific differences (metaphysis over diaphysis or
289 epiphysis) and anatomic differences (tibia metaphysis vs. femur metaphysis) in bone
290 (re)modeling as shown previously[20] that could be a driver for metastasis.
291 To detect and track the location and growth of early metastatic lesions in cortical bone over time,
292 we developed the new eroded bone patch image analysis tool (open code in GitHub). This
293 allowed us to reliably find cortical osteolytic lesions as small as 0.004 mm^3 and as early as two

294 weeks after cancer cell injection (first time point measured). The tool was tested with PBS-
295 injected control animals for up to six weeks post-injection, to rule-out the detection of
296 physiological erosion patches. A similar tool was developed in the past by Campbell et al., where
297 a distance transformation was used to detect lesions with a lowest distance of 150 μm for all
298 planes (in x, y and z)[23], omitting the specific characteristic of lesions to grow across the cortical
299 thickness (in x and y, to a lesser extent in z). In addition, their tool was not tested on healthy
300 mice that undergo major (re)modeling especially at early ages (before 12 weeks). Our eroded
301 bone patch analysis tool has proven reliable in finding early small osteolytic lesions and,
302 importantly, without detecting physiological eroded bone patches. We identified two different
303 kinds of osteolytic lesions in cortical bone: on the periosteal bone surface and in the endocortical
304 region. The majority of cortical lesions initiated at the periosteal side (n = 5 out of 6). This type
305 of cortical lesion had not been reported in the past. The second type in the endocortical region
306 involved erosion of both cortical and trabecular bone.
307 Next to cortical lesions, we analyzed early osteolytic lesions in trabecular bone. All of the lesions
308 were visually detected two weeks after the cancer cell injection (earliest time point) and were
309 located at the growth plate area, eroding the mineralized primary spongiosa (n = 4, three in the
310 tibia, one in the femur). The growth plate is one of the most (re)modeled areas within the bone,
311 and in particular in the tibia, as shown in our previous study with a quantitative analysis of
312 spatial gradients in metaphyseal bone (re)modeling in tibia vs. femur[20]. This further supports the
313 idea that local bone (re)modeling could be a driver for metastasis. One limitation in our study is
314 that trabecular lesions were detected visually based on of both original microCT images and
315 microCT-based time-lapse morphometry; the new eroded bone patch image analysis tool is only
316 applicable to cortical bone. This probably led to an underestimation of trabecular lesions. The

317 results we have shown here and the techniques established for cortical bone are promising for
318 future development of additional tools to (semi)automatically detect osteolytic lesions in
319 trabecular bone, which has a more complex geometry and undergoes more (re)modeling than
320 cortical bone[20].
321 Upon detection and 3D localization of microscopic metastatic lesions as early as two weeks after
322 cancer cell injection, we were able to perform multiscale correlative characterization of the
323 organic and inorganic ECM at the onset of metastatic lesions. As representative regions, we
324 chose a cortical lesion starting at the periosteum and a trabecular lesion adjacent to the growth
325 plate (Fig. 6). Those early lesions first identified with *in vivo* microCT-based time-lapse
326 morphometry, were then captured on exposed 2D bone surface with controlled-angle cutting[24]
327 and confirmed with BSE microscopy of the exposed 2D bone surface. Previous work focusing on
328 skeletal metastatic lesions showed animals with massive lesions, where much of the mineralized
329 tissue had been eroded 4-6 weeks after injection and, hence, no clear analysis of the onset of the
330 lesion could be made[11]. Combining BSE with rhodamine staining and CLSM, as well as SHG
331 imaging, we were able to show that even in small bone metastatic lesions, the collagen fibers and
332 the entire mineralized tissue were resorbed. As a consequence, important structures of the
333 lacuno-canalicular network were disrupted, especially in the case of cortical lesions, spanning the
334 entire cortical thickness. The lacuno-canalicular network plays a key role in bone
335 mechanosensation through fluid flow patterns[25]. Both the disruption of signaling through the
336 lacuno-canalicular network and osteocyte apoptosis have a dramatic impact in bone
337 mechanosensation of the damaged regions and beyond, as network signal propagation is
338 interrupted[26]. In addition, osteocytes that would be buried inside mineralized tissue now become
339 exposed and could get hijacked by tumor cells[27]. To sum up, combining advanced multimodal

340 3D imaging and *ex vivo* correlative tissue characterization, we could detect, localize and
341 characterize alterations of the ECM at the onset of small bone metastatic lesions.
342 Besides the metastatic lesions, we also investigated the proliferative status and localization of
343 disseminated breast cancer cells in the bone marrow. High proliferation is a sign for an
344 outgrowing metastasis, often stained with Ki67 proliferation marker. Miller et al. showed that the
345 absence of Ki67 is a clear signal that a cell is in G0/G1 phase[28]. Therefore, Ki67 is an important
346 indicator of the proliferative status of single breast cancer cells and small clusters. We found that
347 only half of the cell clusters analyzed had one or more $Ki67^{+}$ cell; the other half were entirely
348 $Ki67^{-}$. This is in agreement with previous studies describing the bone marrow as a quiescence-
349 inducing niche[29]. In addition, breast cancer cells and small clusters were found to be located
350 close to and within capillaries and blood vessels, with only few cells located further away. This
351 is also in agreement with previous work showing that breast cancer cells in the bone marrow
352 preferentially co-localize to blood vessels compared to osteoblasts or megakaryocytes[29]. The
353 perivascular niche has been described as both activating and dormancy inducing[29,30], while
354 others have proposed the endocortical niche as quiescence inducing, following the mechanisms
355 of hematopoietic stem cells[31]. Our 3D LSFM visualization shows that $eGFP^{+}$ bone-tropic breast
356 cancer cells and small clusters (>5,500 of 5 different bones) are located close to the endosteal
357 bone surface, while the 2D immunofluorescence analysis locates them in proximity with
358 capillaries and blood vessel. Since recent work revealed that cortical bone is highly vascularized
359 by transcortical vessels[15], the endocortical and perivascular niche can spatially overlap and is
360 therefore difficult to separate between the two.
361 Finally, we studied the altered bone (re)modeling in tumor-injected animals without detectable
362 osteolytic lesions for up to five weeks post injection, to investigate the systemic effect of

363 circulating breast cancer cells or established metastases in other regions. Trabecular bone in both
364 femur and tibia showed significantly increased mineralization in volume and surface at later time
365 points (31 days onward). The differences were more pronounced in the tibia, which is also more
366 (re)modeled in the physiological state[20]. In addition, we found that the erosion is slightly down
367 regulated in the tibia, in particular in the MRR. These findings show a clearly different trend
368 compared to animals with large osteolytic disease[19]. Similar observations were reported by
369 Chiou *et al*, who showed increased bone mineralization in animals injected with tumor
370 conditioned media, suggesting that the increased mineralization is not caused by direct cancer
371 cell contact; instead it could precede osteolytic disease[8]. The mechanism behind remains unclear,
372 with arguments in favor of the premetastatic[8] vs. anti-metastatic niche[32].
373 In summary, using tissue clearing of 3D (intact) bones and LSFM we showed that breast cancer
374 cells and small clusters home in all bone compartments, with a preference for small clusters in
375 the bone marrow and larger clusters on the periosteum. Osteolytic lesions, on the other hand,
376 occurred only in characteristics locations of high bone (re)modeling in the metaphysis. Based on
377 *in vivo* microCT-based time-lapse morphometry and a new image analysis tool, we detected
378 three types of lesions: cortical lesions on the periosteal side, lesions in the endocortical bone
379 propagating to trabecular bone, and trabecular lesions adjacent to the growth plate. These
380 findings support the hypothesis that dynamic bone (re)modeling is a driver for metastasis and
381 gives breast cancer cells the ability to establish an osteolytic bone disease, as cancer cells reach
382 every bone compartment, yet lesions only occur in regions of high bone (re)modeling in the
383 metaphysis. Furthermore, a multiscale correlative tissue characterization of early small bone
384 metastatic lesions showed that not only the mineral but also the collagen fibers are fully
385 resorbed, causing severe changes in the osteocytes and the lacuno-canalicular network. The

386 cellular analysis revealed that half of the breast cancer cells and clusters in the bone marrow are
387 non-proliferative and located close or even within blood vessels. Further, we showed that bone
388 (re)modeling is altered in the absence of visible osteolytic lesions, leading to higher
389 mineralization. Our work provides novel insights of breast cancer cell homing to bone and
390 important 3D dynamic information of bone (re)modeling in the onset of early osteolytic lesions,
391 metastasis initiation and progression.
392

393 **Materials and Methods**

394 **Animal model**

395 12-week-old female BALB/c nude mice (CAnN.Cg-Foxn1nu/Crl, Charles River, Sulzfeld,
396 Germany) were received and acclimatized in the animal facility of the Charité -
397 Universitätsmedizin Berlin. The mice were housed 2-4 animals per cage with ad libitum access
398 to food and water. A reference microCT scan was acquired at day 0 and mice were injected after
399 4 days, under ultrasound guidance (Vevo2100, FUJIFILM VisualSonics Inc., Canada), into the
400 left ventricle of the heart (one injection per mouse) using a 27G needle (Fig. S3A). The control
401 mice (n=10) were injected with PBS to ensure compatibility after this stressful procedure, with 3
402 animals being sacrificed at day 17 for better comparison with tumor animal and *ex vivo*
403 experiments, keeping the age of the animals and the exposure to microCT radiation as similar as
404 possible. The tumor animals (n = 11) were injected with MDA-MB-231-1833 BoM cells ($5x10^5$
405 in 100 µL ice cold PBS). The animals received Carprofen (CP-Pharma Handelsgesellschaft
406 mbH, Burgdorf, Germany) and Buprenorphin (CP-Pharma Handelsgesellschaft mbH, Burgdorf,
407 Germany) as analgesic drugs while under anesthesia. During longitudinal *in vivo* imaging and the
408 intracardiac injection animals were anesthetized using isoflurane (CP-Pharma

409 Handelsgesellschaft mbH, Burgdorf, Germany) at 1-2% with oxygen as a carrier, and the eyes
410 were protected from drying with Pan-Ophtal gel (Dr. Winzer Pharma GmbH, Berlin, Germany).
411 The initial average animal weight was 19.7 g ± 1.7 g for control animals and 20.3 g ± 1.9 g for
412 tumor animals. The weight at sacrifice was: 19.6 g ± 2.1 g after 45 days and 19.5 g ± 0.6 g after
413 17 days. The weight at sacrifice for the tumor animals was 19.2 g ± 2.0 g after 17 to 38 days. All
414 animal experiments were carried out according to the policies and procedures approved by local
415 legal research animal welfare representatives (LAGeSo Berlin, G0224/18).
416
417 **Cell culture**
418 MDA-MB-231-1883 BoM cells were provided by Dr. Joan Massagué and purchased from the
419 Antibody and Bioresource Core Facility of the Memorial Sloan Kettering Cancer Center, USA[33].
420 Briefly, MDA-MB-231 (ATCC ® HTB-26™) human epithelial breast cancer cells were stably
421 transduced with a lentivirus expressing a triple-fusion reporter, forming MDA-MB-231 TGL
422 cells[34]. The here used subclone 1833 is a bone-tropic human cell line deriving from a metastasis
423 formed by these MDA-MB-231 TGL cells hosted in a mouse. MDA-MB-231-1883 BoM cells
424 were cultured in low glucose Dulbecco's Modified Eagle's Medium (DMEM) (Sigma-Aldrich,
425 Taufkirchen, Germany) supplemented with 1% penicillin/streptomycin (Gibco) and 10% fetal
426 bovine serum (FBS superior, Sigma-Aldrich, Taufkirchen, Germany). The cells were grown at
427 37 °C with 5% CO_2 and regular passaging.
428
429 ***In vivo* microCT time-lapse image acquisition**
430 Longitudinal imaging of the hind limbs of the mice was performed with a high resolution
431 microCT (U-CTHR, MILabs, Netherlands). The X-ray tube was operated at 50 kVp source

432 voltage and 210 mA source current. Images were acquired at a step angle of 0.375° with 2
433 projections per step (75 ms exposure time), over a range of 360° and with 8.5 µm voxel size.
434 Two aluminum filters with 100 µm and 400 µm thickness were used. The scan region included
435 the entire femur and tibia of both hind limbs and was determined on an X-ray scout view. To
436 prevent motion artifacts and ensure reproducibility, the anesthetized mice were positioned using
437 an animal bed with the hindlimbs restrained. The scans were reconstructed using the MILabs
438 Reconstruction software and a projection filter (Hann) was applied in the process to limit
439 blurring. The scanner was calibrated before every scan using the internal calibration system. The
440 animals were scanned with the microCT for a reference scan (day 0, 12-week-old). After 17
441 days, the animals were scanned twice per week up until maximum 45 days (on days 17, 20, 24,
442 27, 31, 34, 38, 41 and 45) (Fig. S3A). Anesthetized mice were sacrificed by cervical dislocation.
443 The hind limbs were harvested and fixed with 4% paraformaldehyde (PFA) in PBS over night at
444 4 °C and stored in PBS until further processed.
445
446 ***In vivo* microCT-based time-lapse morphometry**
447 The analysis was performed in accordance with Birkhold et al.[21,35] and Young et al.[20]. To assess
448 morphological changes, microCT scans of each time point (day 17, 20, 24, 27, 31, 34, 38, 41 and
449 45) were compared to the reference scan at day 0, which ensures full information for all time
450 points and no loss of events by changing the reference scan. We analyzed both limbs of all
451 animals. The regions of interest (ROIs) were set at the distal femoral metaphysis and the
452 proximal tibial metaphysis, reaching 10% of the bone length. Each region of interest (ROI)
453 started at the end of the non-mineralized growth plate, on the interface where the primary
454 spongiosa of the metaphysis is found, reaching towards the diaphysis. The ROI included both

455 primary and secondary spongiosa of the metaphysis. The entire epiphysis and other connected
456 bones were manually segmented from the metaphysis. The threshold to remove the background
457 was determined using the 3D Otsu-Method [36] (tool provided by the software Amira 2020.1,
458 Thermo Fisher Scientific, MA, USA). A list of all used thresholds is reported in the
459 Supplementary Table S1 – S4 for PBS-injected control animals and in Supplementary Table
460 S5 – S8 for tumor animals.
461 The registration process and following evaluation was performed in accordance with Birkhold et
462 al.[21] and Young et al.[20]. The images were pre-processed and aligned using Amira. During the
463 pre-processing step, the dataset was pre-cropped to the respective ROI. The epiphysis and other
464 connected bones such as the fibula were removed by manual segmentation. Later time point
465 images were registered onto the reference image (day 0) using a 3D rigid registration algorithm.
466 The threshold was used to exclude background noise from the registration, while keeping the
467 grey scale of the respective bone region data set. A hierarchical strategy was chosen for the
468 registration to avoid local minima, starting with coarse resampling and proceeding to finer
469 resolutions under visual control to ensure correct registration. After the registration, the images
470 were transformed into the same coordinate system using a Lanczos interpolation, keeping the
471 voxel size constant. The images were then re-cropped according to the corresponding ROI.
472 Next, the ROIs were segmented into trabecular and cortical bone using morphological operations
473 as described by Birkhold et al.[21] and evaluated, both using custom-made MATLAB (MATLAB
474 2018a; The Mathworks, Inc. Natick, MA, USA) scripts (Fig. S3B). Bone morphological changes
475 were evaluated as previously described by Young et al[20]: MV/BV (normalized parameters are
476 divided by the respective bone volume or bone surface of the reference scan), normalized
477 mineralized bone surface-to-soft tissue interface (MS_{ST}/BS), normalized mineralized bone

478 surface-to-constant bone interface (MS_{CB}/BS), MAR (mean thickness of formed bone in
479 µm/day), EV/BV, normalized eroded bone surface-to-soft tissue interface (ES_{ST}/BS) normalized
480 eroded bone surface-to-constant bone interface (ES_{CB}/BS), as well as MRR (mean depth of
481 resorbed bone in µm/days). For each case, only the concerning voxels labeled as constant,
482 mineralized or eroded voxels, were taken into consideration. The first layer of voxels was
483 disregarded due to partial volume effects. The second most outward layer of voxels was
484 considered as the soft tissue interface, while the constant bone interface was evaluated by
485 expanding the constant bone surface by one voxel. The description of the surfaces did not
486 influence the analysis of volumetric parameters, which were calculated from all bone voxels
487 independently. A list of all parameters is provided in Supplementary Table S9.
488
489 **Eroded bone patch image analysis tool to detect and track osteolytic lesions in cortical bone**
490 To detect and track the growth of osteolytic lesions in cortical bone with dynamic microCT-
491 based time-lapse morphometry data, a new image analysis tool was developed that could
492 differentiate between physiological and pathological erosion patches in cortical bone.
493 Only eroded voxels of previously segmented cortical bone were considered. A chosen 3D
494 neighborhood of each eroded voxel was evaluated, and the status of surrounding voxels – being
495 eroded or not eroded – plus the voxel itself were considered leading to a sum matrix. Two
496 different empirically determined thresholds were applied a) to analyze the volume of the entire
497 eroded bone patch and b) to detect the eroded bone patch core (main criteria to identify a lesion)
498 To analyze the volume of the eroded bone patch, the noise in form of scattered eroded voxels
499 around the eroded bone patch core was filtered: To do so, the neighborhood of each eroded voxel
500 was explored in 3 voxels in positive and negative x-, y- and z-direction. If a threshold of 70%

501 was fulfilled, those erosion voxels were maintained and contributed to the volume of the eroded
502 bone patch. The threshold parameters were determined empirically under visual control. To
503 detect the eroded bone patch core of only pathological erosions, the neighborhood of each eroded
504 voxel was explored in 9 voxels in positive and negative x- and y-direction and in 4 voxels in
505 positive and negative z-direction. If a threshold of 92.61% was fulfilled, meaning that 92.61% of
506 the neighborhood voxels were erosion voxels, that voxel was identified as belonging to the
507 eroded bone patch core. The parameters were determined empirically ensuring that no lesions
508 were detected in PBS-injected control animals. Only erosion patches containing a core were
509 identified as pathological eroded bone patches. The volume of each eroded bone patch in mm^3
510 was obtained at different time points. The location of osteolytic lesions was visualized with the
511 eroded bone patch core shown in pink and the respective entire patch in green.
512

513 **Lesion analysis in trabecular bone**

514 Trabecular osteolytic lesions were detected visually both in the raw data and the microCT-based
515 time-lapse morphometry data. A region was considered as a lesion if the mineralized part of the
516 growth plate was fully resorbed, leaving an abnormal hole in the spongy structure of the
517 mineralized growth plate.
518

519 **Code availability**

520 The original code as well as the modified version used in this study are available on GitHub:
521 https://github.com/BWillieLab/Timelapse-Morphometry (original code, Birkhold et al.[21,35])
522 https://github.com/CipitriaLab/Timelapse-Morphometry (modified code used in this and the
523 previous study, Young et al.[20])

524 https://github.com/CipitriaLab/Timelapse-Morphometry/tree/lesion_analysis (eroded bone patch
525 image analysis tool developed in this study)
526
527 **Tissue clearing and optical light-sheet fluorescence microscopy (LSFM)**
528 Fixed tibiae were dehydrated in an ascending ethanol series (50, 70 and two times in 100%) for
529 12 h each at room temperature and cleared with ethyl cinnamate (Sigma-Aldrich, Taufkirchen,
530 Germany) at room temperature for 24 h according to the simpleCLEAR protocol[15] (Fig. S3C).
531 To image cleared tibiae via LSFM, a LaVision BioTec Ultramicroscope Blaze
532 (Miltenyi/LaVision BioTec, Bielefeld, Germany) with a supercontinuum white light laser (460 –
533 800 nm), 7 individual combinable excitation and emission filters covering 450 – 865 nm, an
534 AndorNeo sCMOS Camera with a pixel size of 6.5 μm^3, and 1.1× (NA 0.1), 4× (NA 0.35), 12×
535 (NA 0.53) objectives, with a magnification changer ranging from 0.66× to 30× was used. For
536 image acquisition, cleared samples were immersed in ethyl cinnamate in a quartz cuvette and
537 excited at 470/30 nm for eGFP-excitation and 560/40 nm for tissue autofluorescence excitation.
538 eGFP was detected using a 525/50 nm band-pass emission filter and a 620/60 nm band-pass
539 emission filter was used for tissue autofluorescence detection. Because the excitation optics of
540 the microscope provide a light-sheet thickness of 4 – 24 µm (adjustable NA), the Z-step size was
541 set to 5 or 10 µm depending on the selected light-sheet NA. The optical zoom factor varied from
542 1.66× to 4× depending on the objectives and digital zoom factors used.
543 Imaris (Bitplane, Version 9.6.0, Oxford Instruments, Abingdon, UK) was used for data analysis.
544 The bone marrow was segmented manually and the cells were analyzed using the spots tool with
545 an initial estimated diameter of 35.5 µm that was found by manually measuring around 10 cells.
546 n = 5 bones from five different animals were analyzed.

547 The clearing protocol was reversed by placing samples in a descending ethanol series (100, 70,
548 50%) with 1% Tween-20 for 5 h at room temperature each, followed by two steps in PBS with
549 1% Tween-20 (5 h at room temperature each). The samples were stored in PBS until further use.
550

551 **Resin embedding of mineralized bone tissue**

552 Bone specimens were cold embedded at 4 °C in poly(methyl methacrylate) (PMMA) (Technovit
553 9100, Kulzer, Germany), following the manufacturer's instructions. Briefly, samples were
554 dehydrated in an ascending ethanol series (70, 80, 96 and 100%) for 48 h at 4 °C each with a
555 final step in rhodamine solution (4.17 mg/mL−1 Rhodamine B, pure in 100% ethanol, ACROS
556 Organics, Geel, Belgium), followed by a xylene washing, pre-infiltration and infiltration, each
557 for 48 h at 4 °C, and final embedding in PMMA[24].
558

559 **Sectioning using *ex vivo* microCT and controlled angle cutting**

560 In order to expose the metastatic osteolytic lesion, we used controlled angle cutting as described
561 by Moreno-Jimenez et al.[24]. The excess PMMA was first trimmed and the entire block scanned
562 with an *ex vivo* microCT scanner (EasyTom micro/nano tomograph RX solutions, France) at a
563 low resolution with 15 µm voxel size and acquisition parameters of 107 kV, 93 µA, frame rate of
564 6 and average frame of 5. Reconstruction of the 800 projections/scan were performed using RX
565 Solutions X-Act software. The cutting plane to capture the metastatic osteolytic lesion was found
566 using Data Viewer (Bruker, Kontich, Belgium). For small correction angles under 20°, a tilted
567 cylinder was cut and the sample blocks were fixed on it for sectioning. For larger correction
568 angles over 20°, an additional cut of the block was performed with a diamond wire saw
569 (DWS.100, Diamond WireTec GmbH & Co.KG, Weinheim, Germany) and a second microCT

570 scan was performed, repeating the same procedure as above. The histological sections were
571 taken at a thickness of 6 µm with a microtome (Leica RM2255 Microtome, Leica Biosystems,
572 Wetzlar, Germany).
573
574 **Haematoxylin and eosin staining of PMMA sections**
575 The PMMA embedded sections were stained using a standard protocol of haematoxylin and
576 eosin (H&E) (H&E Rapid kit, Clin-Tech, Surrey, UK). In short, samples were rehydrated in a
577 descending ethanol series, followed by staining in Carazzi's double-strength haematoxylin. After
578 another wash in tap water, the slides were stained in eosin, rinsed in tap water, dehydrated in an
579 ascending ethanol series (70, 80, 96, 100% twice for 2 min each), incubated in xylene twice for
580 2 min and mounted (VITROCLUD, deltalab, Barcelona, Spain). The stained sections were
581 imaged with a Keyence Digital Microscope (VKX-5550E, Keyence, Germany). Mineralized
582 tissue and nuclei are shown in dark purple, while soft tissue is shown in light purple.
583
584 **Confocal laser scanning microscopy (CLSM) of PMMA block surface**
585 After sectioning, the exposed PMMA block surface was polished (PM5, Logitech, Glasgow,
586 Scotland) with abrasive paper with grading 4000, and diamond spray with grading of 5 µm, 3 µm
587 and 1 µm, under constant visual control, ensuring that only minimal tissue got removed. The
588 block surface of the rhodamine-stained samples was imaged using CLSM (Leica TCS SP8 DLS,
589 Multiphoton, Leica Microsystems CMS GmbH, Wetzlar, Germany). The samples were imaged
590 with a HC PL APO CS2 40×/1.30 oil objective (NA 1.3) at a magnification of 40×. Argon laser
591 light with $\lambda_{excitation}$ = 514 nm / $\lambda_{emission}$ = 550 – 650 nm was used with a laser intensity of 10%.
592 Images were acquired with a resolution of 1024 x 1024 pixels (pixel size of 284 nm) at a scan

speed of 400 Hz. Over 100 images for each sample with a thickness of 347 nm, spanning a changing thickness of around 50 µm depth from the block surface were imaged. To compensate for the loss of signal with increasing depth, the photomultiplier gain was continuously increased. The images were stitched and visualized with the LAS X software (Version 3.5.7.23225, Leica Microsystems CMS GmbH, Wetzlar, Germany). For each animal, a region containing an osteolytic lesion, either in the cortical or trabecular bone, and a lesion-free region in the same bone at a comparable location were imaged. n = 5 bones from five different animals were analyzed.

Second-harmonic generation (SHG) correlative imaging of PMMA block surface

SHG imaging was performed on the exact same ROI with the same instrument and objective. A pulsed infrared laser ($\lambda_{excitation}$ = 910 nm/ $\lambda_{emission}$ = 450 – 460 nm) with a power of 0.6 W and an intensity of 10% was used. Images were acquired with a resolution of 1024 x 1024 pixels (pixel size of 284 nm) at a scan speed of 400 Hz. Around 20 images with a thickness of 2.8 µm were acquired, keeping the same total depth as the previous rhodamine- stained fluorescence imaging. For each animal a region containing an osteolytic lesion, either in the cortical or trabecular bone, and a lesion-free region at a comparable location were imaged. The images were stitched and visualized with the LAS X software (Version 3.5.7.23225, Leica Microsystems CMS GmbH, Wetzlar, Germany). n = 5 bones from five different animals were analyzed.

Backscattered electron (BSE) correlative imaging of PMMA block surface

BSE imaging was performed on the exact same ROI with an environmental scanning electron microscope (Quattro ESEM, Thermo Fisher Scientific, Waltham, US). The following settings

616 were used: 15 kV, low vacuum conditions (100 Pa), working distance of approximately 8 mm,
617 spot size of 3 and 500× magnification. The images were manually stitched using Adobe
618 Photoshop 2022. n = 5 bones from five animals were analyzed.
619
620 **Cryo-embedding and -sectioning of mineralized bone tissue**
621 Bones of one limb of each mouse without a detectable osteolytic lesion were freeze-embedded
622 following the method of the SECTION-LAB Co. Ltd. (Hiroshima, Japan). Briefly, the samples
623 were dehydrated in an ascending sucrose solution (10, 20 and 30% in distilled water) for 24 h
624 each at 4 °C. Next, a metal mold was placed in isopropanol, cooled with liquid nitrogen and
625 filled with embedding medium (SCEM; SECTION-LAB Co. Ltd., Hiroshima, Japan). The bone
626 was placed in the middle and covered with embedding medium, avoiding direct contact with the
627 cooled isopropanol. Samples were stored at −80 °C until further use. Cryosections with a
628 thickness of 20 µm were cut following the Kawamoto method using a cryostat (Leica CM3060S,
629 Leica Microsystems CMS GmbH, Wetzlar, Germany). The sections were collected using
630 Kawamoto films (type 2C(9), SECTION-LAB Co. Ltd., Hiroshima, Japan), then attached to a
631 microscopic slide and stored at -20 °C until further use.
632
633 **Immunofluorescence staining and imaging of cryosections**
634 For IF staining, the slides were blocked with blocking buffer (1% bovine serum albumin (BSA),
635 Sigma-Aldrich, Taufkirchen, Germany, 0.1% Tween20 Carl Roth, Karlsruhe, Germany, 0.1%
636 dimethyl sulfoxide (DMSO), Merck KGaA, Darmstadt, Germany in PBS) for 1 h. Primary and
637 secondary antibodies were diluted in blocking buffer and incubated for at least 4 h at room
638 temperature or overnight at 4 °C, with in between washing steps (three times, 15 min each) in

639 washing buffer (0.1% Tween20, 0.1% DMSO in PBS). Final washing steps were conducted in
640 washing buffer (twice for 15 min) and in distilled water (once for 15 min). Slides were then
641 mounted with Dako fluorescence mounting media (S302380-2, Agilent Technologies, Santa
642 Clara, US). The primary antibodies and respective concentrations used in this study are the
643 following: 4',6-diamidino-2-phenylindole (DAPI) (1:500, Roche), anti-Ki67 (1:100, 14-5698-82,
644 eBioscience™) and anti-CD31 (1:200, 102516, Biolegend). As secondary antibody Alexa Fluor
645 555 (1:1000, 4417S, Cell Signaling Technology) was used. Samples were imaged using CLSM
646 (Leica TCS SP8 DLS, Multiphoton, Leica Microsystems CMS GmbH, Wetzlar, Germany).
647 Three different objectives were used: HC APO L 10x/0.30 water objective (NA 0.3) at a
648 magnification of 10×, HC PL APO CS2 40×/1.30 oil objective (NA 1.3) at a magnification of
649 40×, HC PL APO CS2 63x/1.40 oil objective (NA 1.4) at a magnification of 63×. For imaging
650 the DAPI, diode 405 laser light with $\lambda_{excitation}$ = 405nm / $\lambda_{emission}$ = 410 – 483nm was used. For
651 imaging the eGFP, argon laser light with $\lambda_{excitation}$ = 488nm / $\lambda_{emission}$ = 493 – 556nm was used.
652 For imaging the Alexa Fluor 555, DPSS 561 laser light with $\lambda_{excitation}$ = 561nm / $\lambda_{emission}$ = 566 –
653 756nm laser light was used. For imaging the Alexa Fluor 647, HeNe 633 laser light with $\lambda_{excitation}$
654 = 633nm / $\lambda_{emission}$ = 638 – 755nm was used. Laser intensity and photomultiplier gain were kept
655 constant: DAPI (intensity 1%, HyD detector, gain 30), eGFP (intensity 20%, Hyd SMD 2
656 detector, gain 2900), Alexa Fluor 555 (intensity 1%, PMT detector, gain 650) and Alexa Fluor
657 647 (intensity 3%, HyD detector, gain 200). Images were acquired with a resolution of 1024 x
658 1024 pixels (pixel size of 284 nm) at a scan speed of 400 Hz (200 Hz for 63× magnification). A
659 varying number of images with a thickness of 4 µm (2 µm for 63× magnification) were made
660 over a depth of around 20 µm. For 10× and 40× magnification, tile scans were acquired
661 depending on the size of the sample.

662 Images were analyzed and visualized with Imaris (Imaris Viewer 9.8.0, Oxford Instruments,
663 Abingdon, United Kingdom). 40× magnification images were used for quantification and the
664 thresholds were applied manually under visual control. For Ki67 analysis, cells/clusters were
665 manually segmented using the surface tool on each layer. Nuclear Ki67 signal was overlapped
666 using the DAPI signal and counted automatically. For distance analysis with CD31, cancer cells
667 were estimated on one layer using the surface tool. CD31 was segmented using the surface tool,
668 distance mapping and overlapping were calculated automatically. n = 3 (Ki67) and n = 4 (CD31)
669 bones from four animals were analyzed.
670

671 **Statistical analysis**

672 In the analysis of altered bone (re)modeling in absence of detectable bone lesions, only bones
673 harvested from animals without detectable osteolytic lesions in the hind limbs were included. All
674 bones harvested from animals with confirmed lesions were excluded from this analysis. Both
675 limbs of all animals were considered, resulting in seven control animals with n = 14 bones and 5
676 tumor animals with n = 10 bones. The plots show the mean and standard deviation. Two sample
677 t-tests were used for statistical comparison between different groups. Significant differences are
678 presented as * $p \leq 0.05$.
679

680 **References**

681 1. Torre, L. A. *et al.* Global cancer statistics, 2012. *CA. Cancer J. Clin.* **65**, 87–108 (2015).
682 2. Coleman, R. E. Clinical Features of Metastatic Bone Disease and Risk of Skeletal
683 Morbidity. *Clin. Cancer Res.* **12**, 6243s-6249s (2006).
684 3. Weilbaecher, K. N., Guise, T. A. & McCauley, L. K. Cancer to bone: a fatal attraction.

685 *Nat. Rev. Cancer* **11**, 411–425 (2011).

686 4. Harbeck, N. *et al.* Breast cancer. *Nat. Rev. Dis. Prim.* **5**, 66 (2019).

687 5. Coleman, R. E. *et al.* Bone metastases. *Nat. Rev. Dis. Prim.* **6**, 83 (2020).

688 6. Phan, T. G. & Croucher, P. I. The dormant cancer cell life cycle. *Nat. Rev. Cancer* **20**,
689 398–411 (2020).

690 7. Croucher, P. I., McDonald, M. M. & Martin, T. J. Bone metastasis: the importance of the
691 neighbourhood. *Nat. Rev. Cancer* **16**, 373–386 (2016).

692 8. Chiou, A. E. *et al.* Breast cancer–secreted factors perturb murine bone growth in regions
693 prone to metastasis. *Sci. Adv.* **7**, 1–14 (2021).

694 9. Crist, S. B. & Ghajar, C. M. When a House Is Not a Home: A Survey of Antimetastatic
695 Niches and Potential Mechanisms of Disseminated Tumor Cell Suppression. *Annu. Rev.*
696 *Pathol. Mech. Dis.* **16**, 409–432 (2021).

697 10. Price, T. T. *et al.* Dormant breast cancer micrometastases reside in specific bone marrow
698 niches that regulate their transit to and from bone. *Sci. Transl. Med.* **8**, 340ra73-340ra73
699 (2016).

700 11. He, F. *et al.* Multiscale characterization of the mineral phase at skeletal sites of breast
701 cancer metastasis. *Proc. Natl. Acad. Sci.* **114**, 10542–10547 (2017).

702 12. Di Martino, J. S. *et al.* A tumor-derived type III collagen-rich ECM niche regulates tumor
703 cell dormancy. *Nat. Cancer 2021* 1–18 (2021). doi:10.1038/s43018-021-00291-9

704 13. Fonta, C. M. *et al.* Fibronectin fibers are highly tensed in healthy organs in contrast to
705 tumors and virus-infected lymph nodes. *Matrix Biol. Plus* **8**, 100046 (2020).

706 14. Grüneboom, A. *et al.* Next-generation imaging of the skeletal system and its blood supply.
707 *Nat. Rev. Rheumatol.* **15**, 533–549 (2019).

708 15. Grüneboom, A. *et al.* A network of trans-cortical capillaries as mainstay for blood
709 circulation in long bones. *Nat. Metab.* **1**, 236–250 (2019).
710 16. Winkler, J., Abisoye-Ogunniyan, A., Metcalf, K. J. & Werb, Z. Concepts of extracellular
711 matrix remodelling in tumour progression and metastasis. *Nat. Commun.* **11**, 5120 (2020).
712 17. Fratzl, P. & Weinkamer, R. Nature's hierarchical materials. *Prog. Mater. Sci.* **52**, 1263–
713 1334 (2007).
714 18. Wang, N. *et al.* The frequency of osteolytic bone metastasis is determined by conditions
715 of the soil, not the number of seeds; evidence from in vivo models of breast and prostate
716 cancer. *J. Exp. Clin. Cancer Res.* **34**, 124 (2015).
717 19. Johnson, L. C. *et al.* Longitudinal live animal micro-CT allows for quantitative analysis of
718 tumor-induced bone destruction. *Bone* **48**, 141–151 (2011).
719 20. Young, S. A. E. *et al.* In vivo microCT-based time-lapse morphometry reveals anatomical
720 site-specific differences in bone (re)modeling serving as baseline parameters to detect
721 early pathological events. *Bone* **161**, 116432 (2022).
722 21. Birkhold, A. I. *et al.* Mineralizing surface is the main target of mechanical stimulation
723 independent of age: 3D dynamic in vivo morphometry. *Bone* **66**, 15–25 (2014).
724 22. Aceto, N. *et al.* Circulating Tumor Cell Clusters Are Oligoclonal Precursors of Breast
725 Cancer Metastasis. *Cell* **158**, 1110–1122 (2014).
726 23. Campbell, G. M. *et al.* Tracking the Progression of Osteolytic and Osteosclerotic Lesions
727 in Mice Using Serial In Vivo µCT: Applications to the Assessment of Bisphosphonate
728 Treatment Efficacy. *J. Bone Miner. Res.* **33**, 410–418 (2018).
729 24. Moreno-Jiménez, I., Garske, D. S., Lahr, C. A., Hutmacher, D. W. & Cipitria, A. Targeted
730 2D histology and ultrastructural bone analysis based on 3D microCT anatomical locations.

731 *MethodsX* **8**, 101480 (2021).

732 25. van Tol, A. F. *et al.* Network architecture strongly influences the fluid flow pattern
733 through the lacunocanalicular network in human osteons. *Biomech. Model. Mechanobiol.*
734 (2019). doi:10.1007/s10237-019-01250-1

735 26. Weinkamer, R., Kollmannsberger, P. & Fratzl, P. Towards a Connectomic Description of
736 the Osteocyte Lacunocanalicular Network in Bone. *Curr. Osteoporos. Rep.* **17**, 186–194
737 (2019).

738 27. Hemmatian, H. *et al.* Reorganization of the osteocyte lacuno-canalicular network
739 characteristics in tumor sites of an immunocompetent murine model of osteotropic
740 cancers. *Bone* 116074 (2021). doi:10.1016/j.bone.2021.116074

741 28. Miller, I. *et al.* Ki67 is a Graded Rather than a Binary Marker of Proliferation versus
742 Quiescence. *Cell Rep.* **24**, 1105-1112.e5 (2018).

743 29. Carlson, P. *et al.* Targeting the perivascular niche sensitizes disseminated tumour cells to
744 chemotherapy. *Nat. Cell Biol.* **21**, 238–250 (2019).

745 30. Ghajar, C. M. *et al.* The perivascular niche regulates breast tumour dormancy. *Nat. Cell*
746 *Biol.* **15**, 807–817 (2013).

747 31. Dhawan, A. *et al.* Breast cancer cells compete with hematopoietic stem and progenitor
748 cells for intercellular adhesion molecule 1-mediated binding to the bone marrow
749 microenvironment. *Carcinogenesis* **37**, 759–767 (2016).

750 32. Kolb, A. D., Shupp, A. B., Mukhopadhyay, D., Marini, F. C. & Bussard, K. M.
751 Osteoblasts are "educated" by crosstalk with metastatic breast cancer cells in the bone
752 tumor microenvironment. *Breast Cancer Res.* **21**, 31 (2019).

753 33. Minn, A. J. *et al.* Genes that mediate breast cancer metastasis to lung. *Nature* **436**, 518–

754 524 (2005).
755 34. Ponomarev, V. *et al.* A novel triple-modality reporter gene for whole-body fluorescent,
756 bioluminescent, and nuclear noninvasive imaging. *Eur. J. Nucl. Med. Mol. Imaging* **31**,
757 740–751 (2004).
758 35. Birkhold, A. I. *et al.* The influence of age on adaptive bone formation and bone resorption.
759 *Biomaterials* **35**, 9290–9301 (2014).
760 36. Otsu, N. A Threshold Selection Method from Gray-Level Histograms. *IEEE Trans. Syst.*
761 *Man. Cybern.* **9**, 62–66 (1979).
762
763
764 **Acknowledgements**
765 This work was funded by the Deutsche Forschungsgemeinschaft (DFG) Emmy Noether grant (CI
766 203/2-1 to A. C., S. A. E. Y., and D. S. G.). A. C. also thanks the funding from IKERBASQUE
767 Basque Foundation for Science and from the Spanish Ministry of Science and Innovation
768 (PID2021-123013OB-I00) (Ministerio de Ciencia e Innovación, la Agencia y del Fondo Europeo
769 de Desarrollo Regional, Proyecto PID2021-123013OB-I00 financiado por
770 MCIN/AEI/10.13039/501100011033/FEDER.UE). A.-D. H. thanks the International Max Planck
771 Research School (IMPRS) on Multiscale Bio Systems for financial support. The FRQS
772 Programme de bourse de chercheur provided support to B.W. We thank the lab of Dr. Joan
773 Massagué at the Memorial Sloan Kettering Cancer Center, USA, for providing the MDA-MB-
774 231-1883 BoM cells. We thank Jeannette Steffen for technical assistance with sectioning and
775 staining. The authors would like to acknowledge Peter Fratzl, Sadra Bakhshandeh and Hubert
776 Taïeb for scientific discussion.

Author contribution

Study design: AC, SAEY

Experimental work: SAEY, DSG, VQ, AE, AC

Data analysis: SAEY, ADH, AG, AC

Visualization: SAEY, ADH, AC

Data interpretation: SAEY, ADH, MR, GND, BMW, AG, AC

Project supervision: AC

Drafting manuscript: SAEY, AC

Revising manuscript content and approving final version: all authors

Competing interests

The authors declare no conflict of interest

Data and materials availability

The MATLAB codes used are freely available in GitHub and the links are provided in the Methods section. The data supporting the findings can be made available upon reasonable request.

Figures

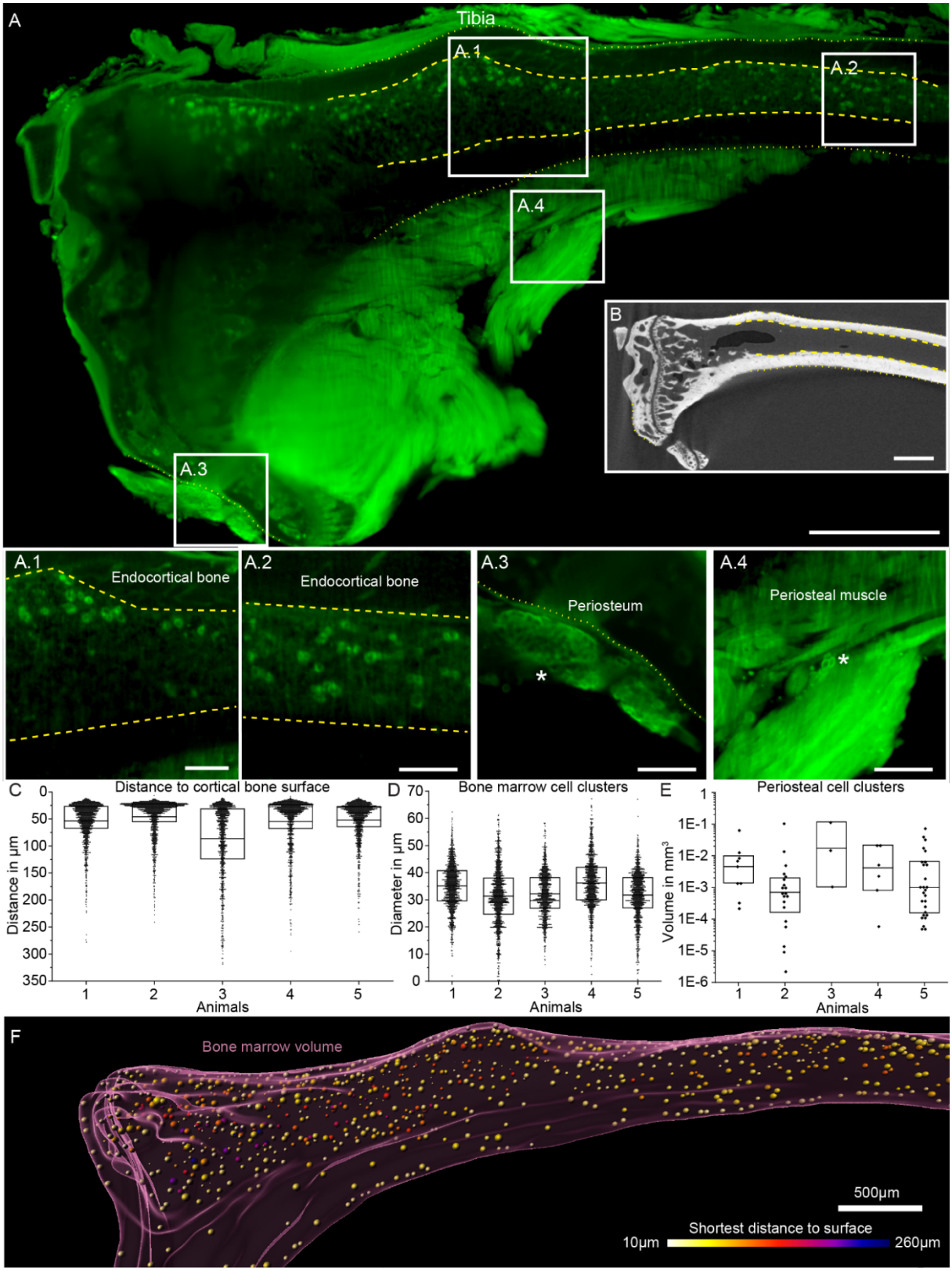
A
Tibia
A.1
A.2
A.3
A.4
B
A.1
Endocortical bone
A.2
Endocortical bone
A.3
Periosteum
A.4
Periosteal muscle
C
Distance to cortical bone surface
Distance in µm
Animals
D
Bone marrow cell clusters
Diameter in µm
Animals
E
Periosteal cell clusters
Volume in mm³
Animals
F
Bone marrow volume
500µm
Shortest distance to surface
10µm
260µm

797 **Fig. 1. Light-sheet fluorescence microscopy (LSFM) and 3D quantification of the size and**
798 **spatial distribution of breast cancer cells and small clusters homing in the bone marrow.**
799 LSFM images of one (virtual) section are depicted for (**A**) one entire bone, with enlargements of
800 small cell clusters in the (**A.1**) bone marrow upper diaphysis with the endocortical bone surface
801 delimited with a dashed yellow line, (**A.2**) bone marrow lower diaphysis, (**A.3**) periosteal site
802 with a large dense cluster (asterisk) and (**A.4**) in between muscle tissue with a small cluster
803 (asterisk). (**B**) MicroCT image of the same (virtual) bone section as shown in A, with highlighted
804 endocortical and periosteal bone surfaces. Quantification of (**C**) the distance to the cortical bone
805 surface and (**D**) the size distribution of breast cancer cells and small clusters. (**E**) Quantification
806 of the volume of larger breast cancer cell clusters on the periosteum. (**F**) Graphical 3D
807 visualization of the distance of breast cancer cells and small clusters to the endocortical bone
808 surface, with the color code indicating the distance. (Asterisks in A.3 and A.4 indicate the
809 presence of cancer cells and scale bars correspond to 500 µm (A and B) and 200 µm (A.1-A.4)
810 respectively. The box plots show the mean (C and D) or median (E) and first and third quartile. n
811 = 5 bones from five tumor animals, representative images from one animal with a trabecular
812 bone lesion).

813

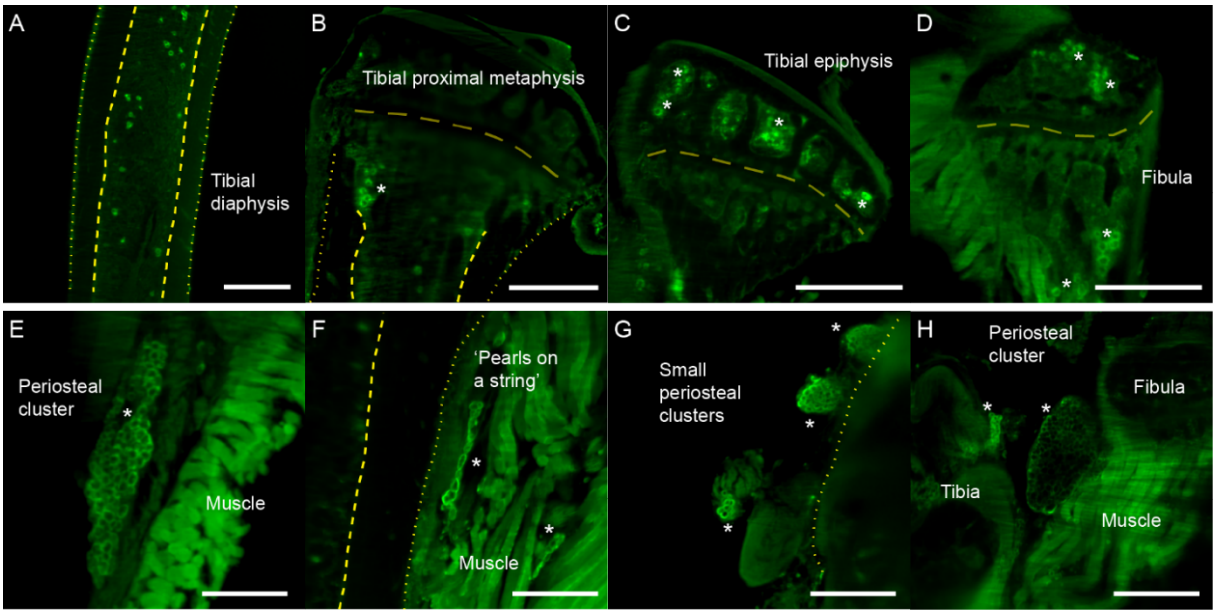

Fig. 2. LSFM visualization of breast cancer cells and small clusters in various compartments of skeletal tissue. Images showing cancer cells in the (**A**) tibial diaphysis, (**B**) tibial proximal metaphysis, (**C**) tibial epiphysis and (**D**) fibula, as well as in the periosteal tissue as (**E**) a large cluster, (**F**) like 'pearls on a string', (**G**) as small clusters and (**H**) as a large cluster between tibia and fibula. (Scale bars correspond to 500 µm (A-D) and 250 µm (E-F), cancer cells and patches are marked with an asterisk; periosteal and endocortical bone, as well as the growth plate are delimited with dashed yellow lines. n = 5 bones from five tumor animals).

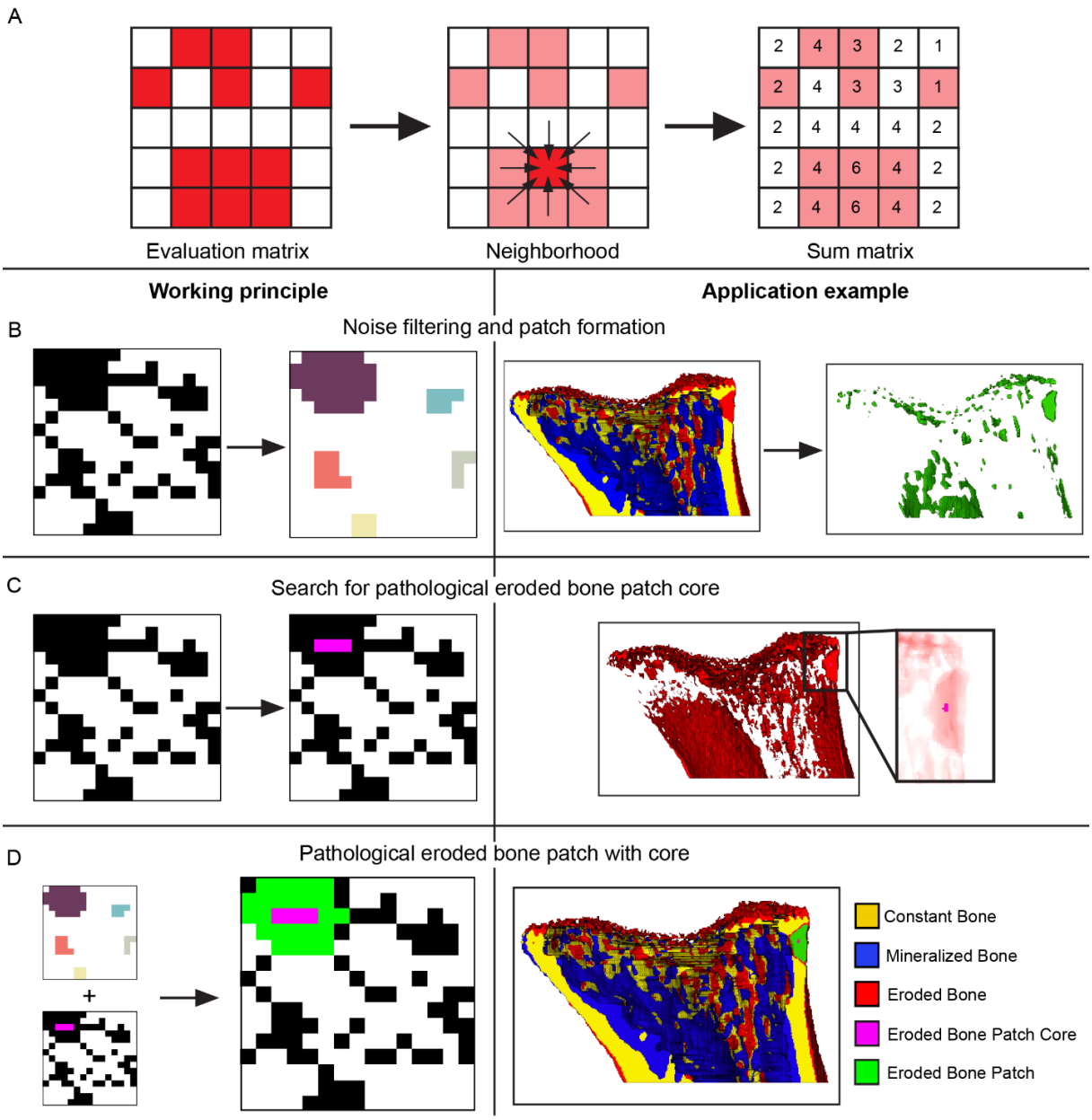

Fig. 3. Eroded bone patch image analysis tool to detect and track the growth of early bone metastatic lesions over time based on in vivo microCT time-lapse morphometry. (**A**) Schematic showing how the neighborhood is determined, starting at the evaluation matrix, with a 2D simplified 3×3 neighborhood for one voxel and the resulting sum matrix for all voxels. Working principle (left) and application example (right) of the eroded bone patch analysis starting with (**B**) filtering of noise to form separate patches, (**C**) search for a pathological eroded

bone patch core and (**D**) determining the volume of the pathological eroded bone patch by matching the filtered patch with the core. Constant bone is shown in yellow, mineralized bone in blue, eroded bone in red, eroded bone patch in green and eroded bone patch core in pink.

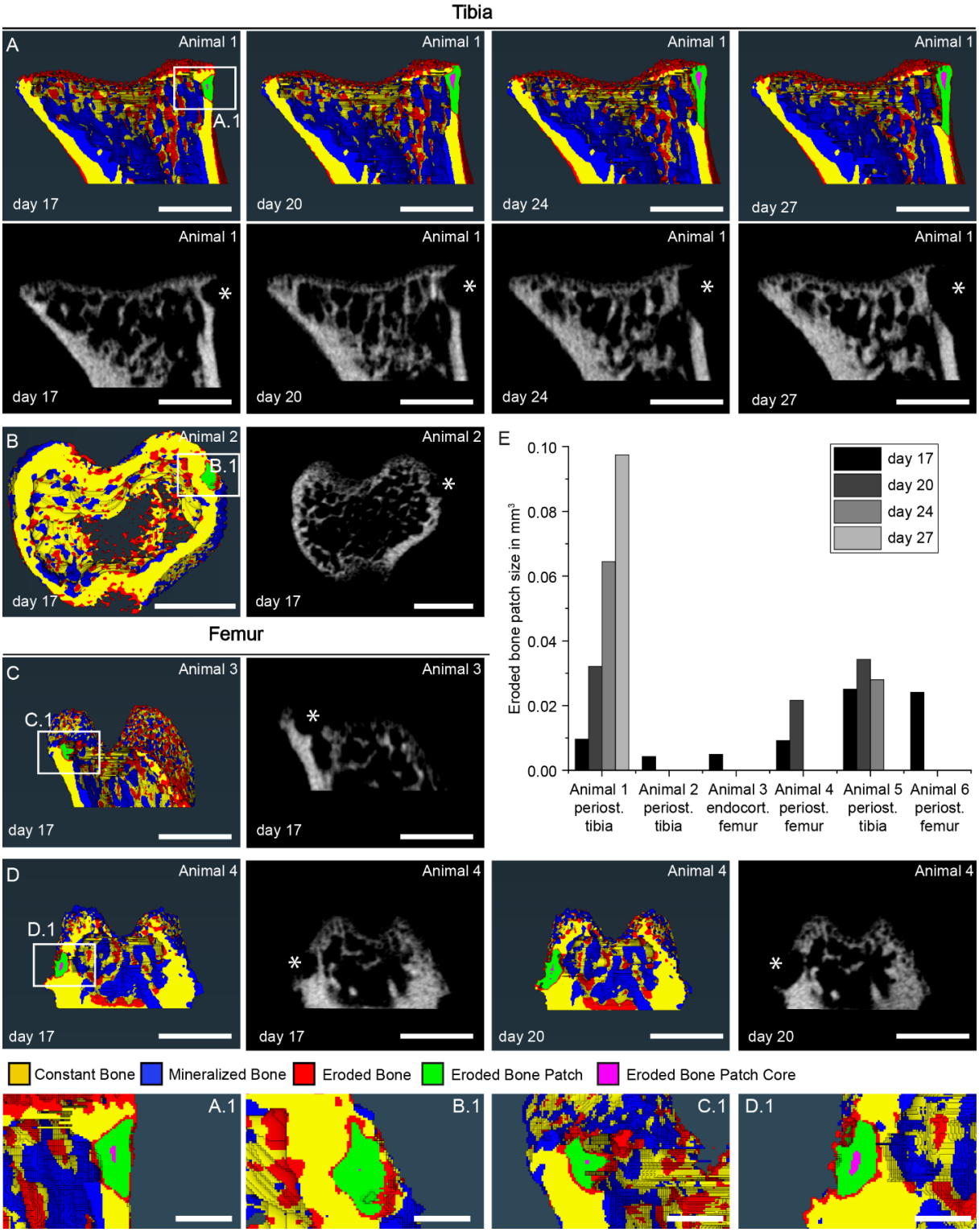

Fig 4. Spatio-temporal analysis of the location and growth of early metastatic lesions in cortical bone using the new eroded bone patch image analysis tool. Results of bone (re)modeling and detection of pathological erosion-patches in the tibia of (**A**) animal 1 at day 17

838 (enlargement in (**A.1**)), day 20, day 24 and day 27, and (**B**) animal 2 at day 17 (enlargement in
839 (**B.1**)). Analogous analysis for the femur of (**C**) animal 3 at day 17 (enlargement in (**C.1**)) and
840 (**D**) animal 4 at day 17 (enlargement in **D.1**) and day 20. (**E**) Quantitative results of the eroded
841 bone patch analysis per animal up to 27 days. (Bone (re)modeling visualization of constant bone
842 in yellow, mineralized bone in blue, eroded bone in red, eroded bone patches in green, eroded
843 bone patch core in pink and respective microCT grey scale images. Scale bars correspond to
844 1 mm, scale bar for enlargements 0.2 mm. The lesions are indicated with an asterisk in the grey
845 scale images. n = 6 bones from six tumor animals).

846

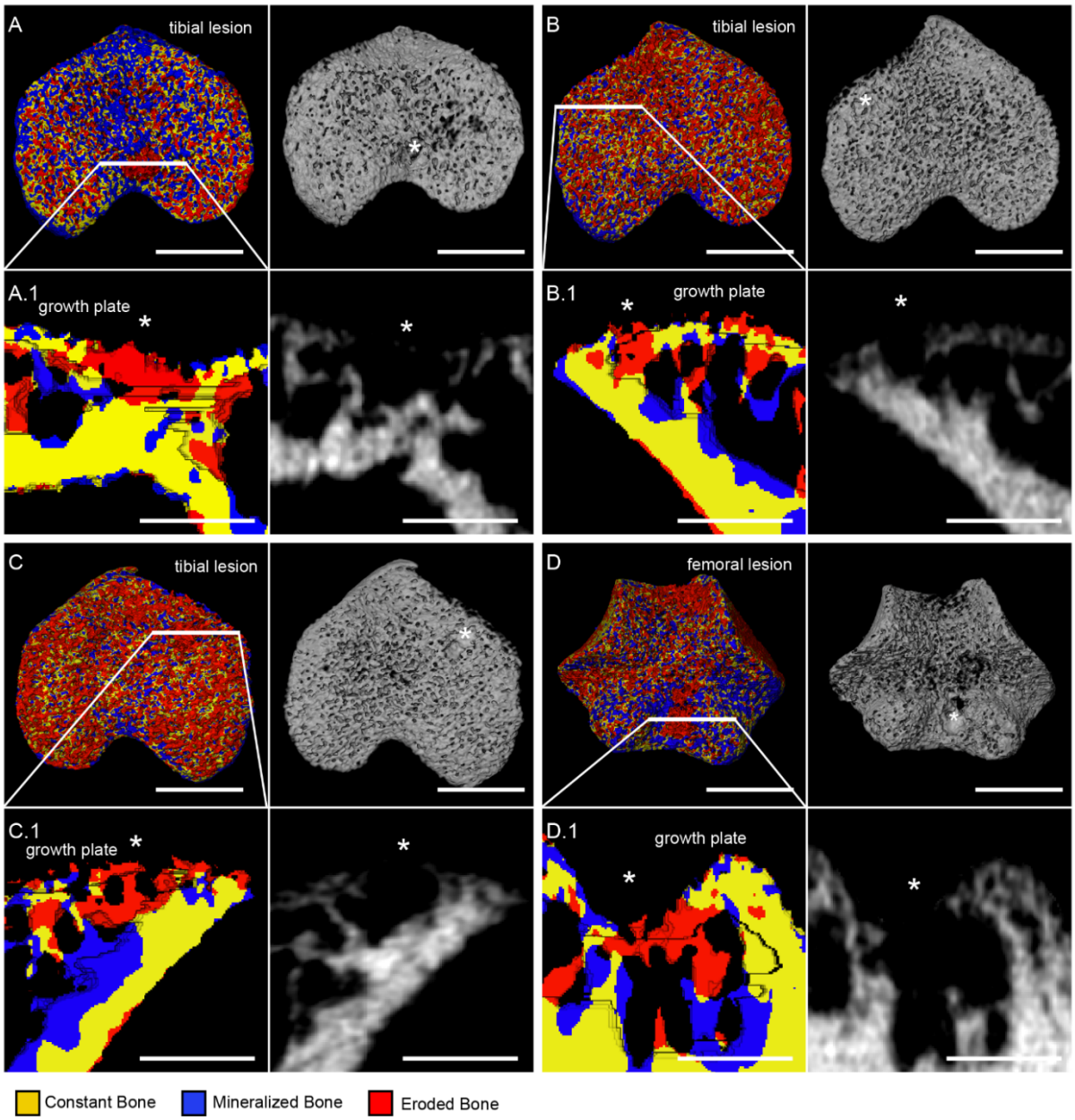

Fig. 5. Early metastatic lesions in trabecular bone initiation at the mineralized growth plate in the primary spongiosa as shown by microCT-based time-lapse morphometry. Results of bone (re)modeling with constant bone in yellow, mineralized bone in blue, eroded bone in red, as well as grey scale images for all bones at day 17. (**A**) (Re)modeling visualization top view, with respective grey scale image and (**A.1**) enlargement of the cross-section of the osteolytic lesion for the left tibia of animal 1. (**B**) Analogous visualization and (**B.1**) enlargement of the cross-section for the left tibia of animal 2. (**C**) Analogous visualization and (**C.1**) enlargement of the

854 cross-section for the right tibia of animal 2. (**D**) Analogous visualization and (**D.1**) enlargement
855 of the cross-section for the right femur of animal 2. (Scale bars correspond to 1 mm and 0.5 mm
856 for enlargements. The lesions are indicated with an asterisk. n = 4 bones from two tumor
857 animals).

858

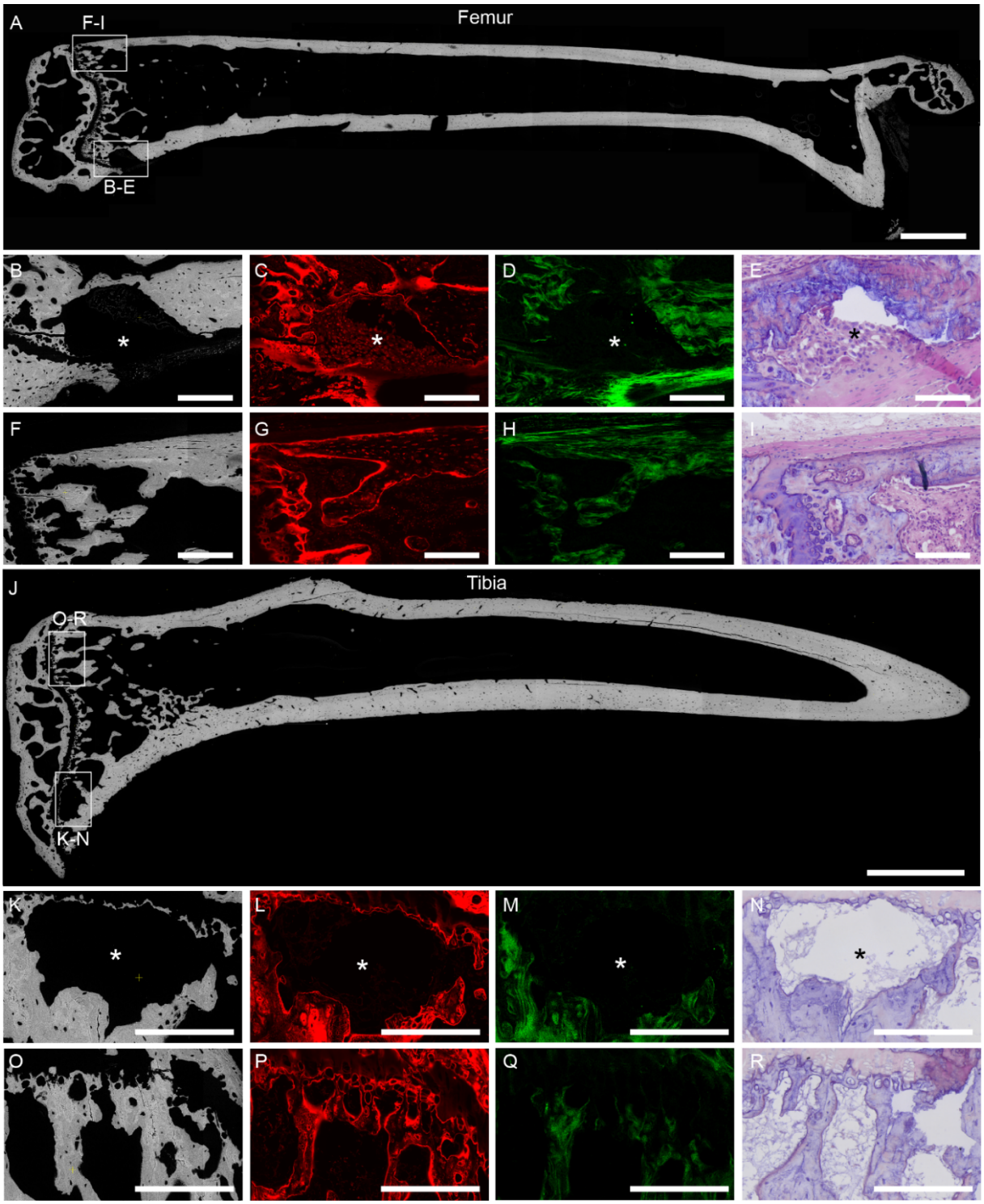

Fig. 6. Multiscale correlative tissue characterization of early metastatic lesions in cortical and trabecular bone and comparison with intact bone tissue in the same sample. (**A**) Overview BSE microscopy image of a femur with (**B**) enlargement of a cortical lesion, as well as

862 (**C**) CLSM of rhodamine-stained tissue, (**D**) SHG imaging of collagen fibers and (**E**) H&E
863 histology. (**F**) BSE microscopy enlargement of an intact bone region, as well as (**G**) CLSM of
864 rhodamine-stained tissue, (**H**) SHG imaging of collagen fibers and (**I**) H&E histology. (**J**)
865 Overview BSE microscopy image of a tibia with (**K**) enlargement of a trabecular lesion, as well
866 as (**L**) CLSM (rhodamine staining), (**M**) SHG imaging of collagen fibers and (**N**) H&E
867 histology. (**O**) BSE microscopy enlargement of a healthy trabecular region, as well as (**P**) CLSM
868 (rhodamine staining), (**Q**) SHG imaging of collagen fibers and (**R**) H&E histology. (Asterisks
869 indicate the presence of a lesion, scale bars correspond to 1 mm and 200 µm in the enlargements.
870 n = 5 bones from five tumor animals containing an osteolytic lesion were analyzed,
871 representative images from two animals shown).

872

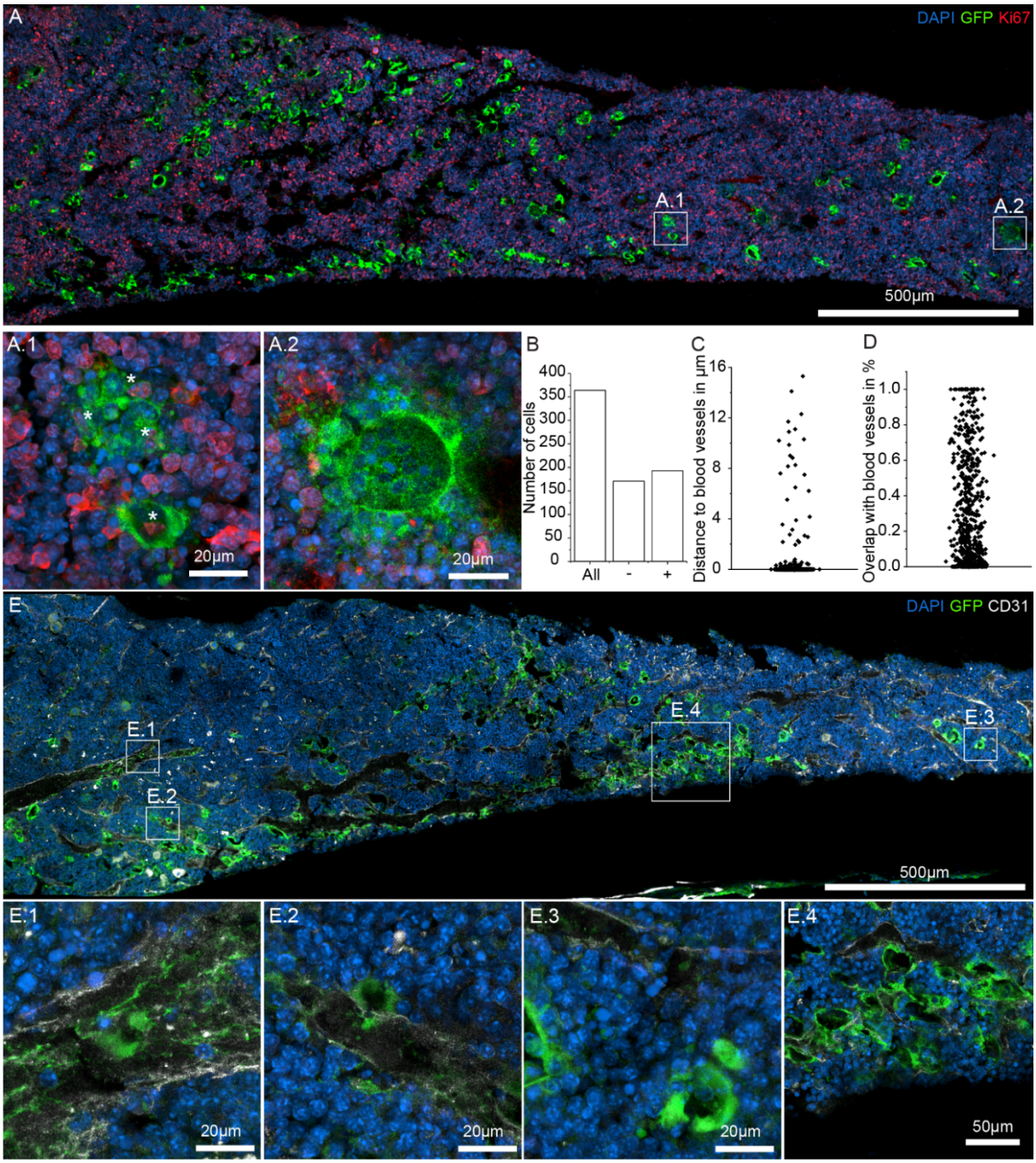

Fig. 7. Breast cancer cells and small clusters are low in proliferation and found in close proximity and inside of blood vessels. (A) CLSM imaging of Ki67 proliferation marker with enlargement (**A.1**) showing a Ki67 positive breast cancer cell cluster and (**A.2**) showing a Ki67 negative breast cancer cell clusters. (**B**) Quantification of the Ki67 signal for all n = 364 analyzed single cells and small clusters. Quantification of breast cancer cell and small cluster (**C**) distance

878 to blood vessels and (**D**) degree of overlap with blood vessels. (**E**) CLSM imaging of CD31 with
879 enlargements showing breast cancer cells and small clusters (**E.1**) inside a blood vessel, (**E.2**) in
880 direct contact with a blood vessel, (**E.3**) with a larger distance from blood vessels and (**E.4**) close
881 to the endosteal bone surface. (Scale bars correspond to 500 µm and 20 µm for the enlargements,
882 except for E.4 with 50 µm. DAPI staining of the nucleus in blue, eGFP of the cancer cells in
883 green, Ki67 in red and CD31 in white. n = 3 bones (Ki67) from three tumor animals and n = 4
884 bones (CD31) from four tumor animals with osteolytic lesions in other long bones).

885

886

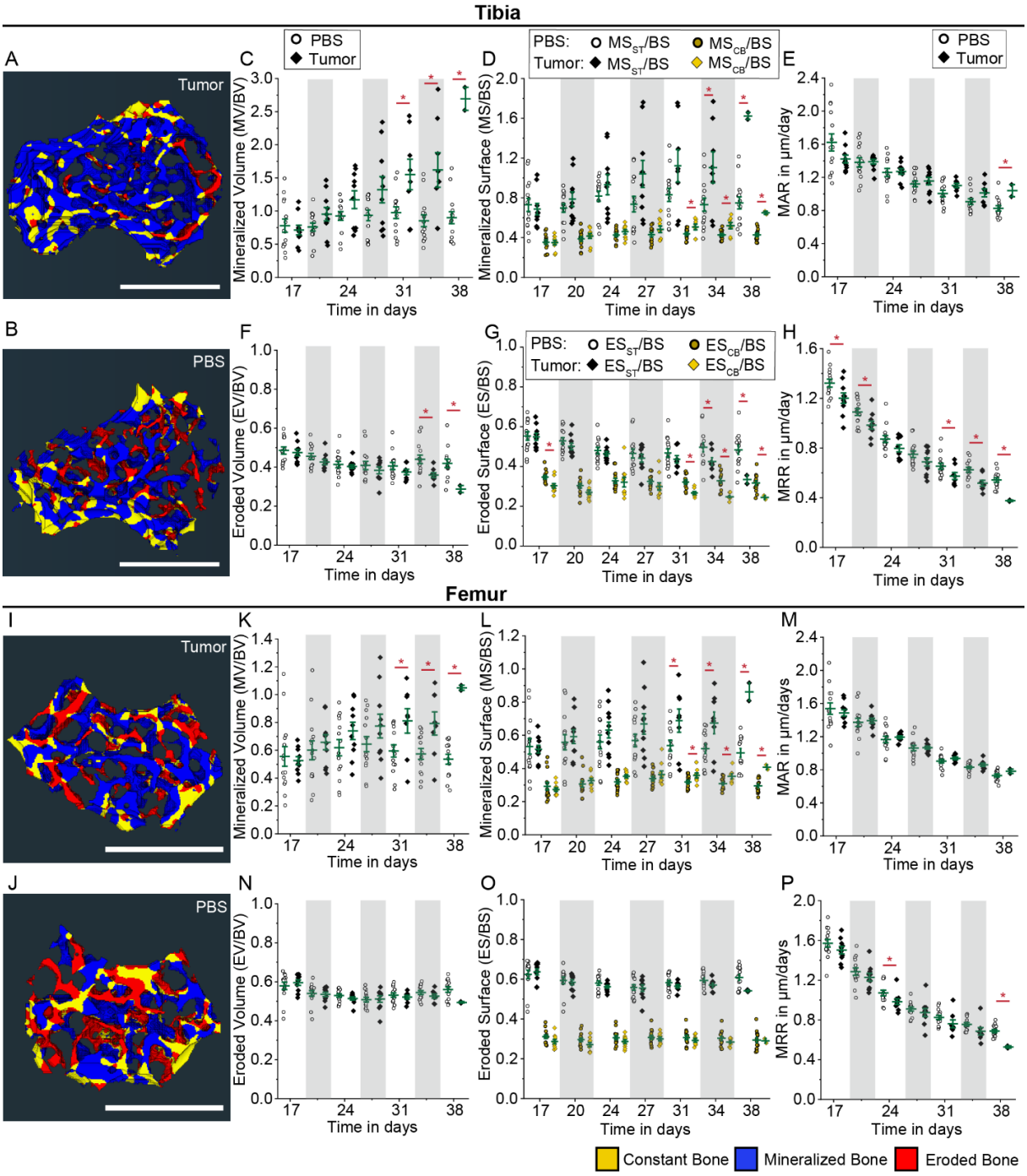

887 **Fig. 8. Altered trabecular bone (re)modeling in absence of detectable bone lesions.** Results
888 in trabecular bone of tibial proximal metaphysis are depicted for (**A**) tumor cell injected animals
889 and (**B**) PBS-injected control animals, with newly mineralized bone in blue, eroded bone in red
890 and constant bone in yellow. Results are shown for mineralization with (**C**) MV/BV, (**D**)
891 MS_{ST}/BS as well as MS_{CB}/BS and (**E**) MAR, as well as erosion with (**F**) EV/BV, (**G**) ES_{ST}/BS as

892 well as ES_{CB}/BS and (**H**) MRR. Analogous analysis for trabecular bone in the femoral distal
893 metaphysis depicted for (**I**) tumor cell injected animals and (**J**) PBS-injected control animals.
894 Results are shown for mineralization with (**K**) MV/BV, (**L**) MS_{ST}/BS as well as MS_{CB}/BS and
895 (**M**) MAR, as well as erosion with (**N**) EV/BV, (**O**) ES_{ST}/BS as well as ES_{CB}/BS and (**P**) MRR.
896 (All plots show mean and standard deviation, with statistically significant values presented as * p
897 ≥ 0.05, a two-sample t-tests was used. Exemplary images were taken from registration data at
898 day 34, scale bars correspond to 1 mm. PBS control group: n = 14 bones from seven animals,
899 Tumor group: n = 10 bones from five animals, for tibia and femur respectively.)